Wide-Angle Frequency Selective Surface with Ultra-Wideband Response for Aircraft Stealth Designs

Boyu Hua[1], Xiaochun Liu[2], Xiaoxiang He[1], and Yang Yang[1, *]

Abstract—An ultra-wideband frequency selective surface (FSS) for wide incident angles is proposed. Its -3 dB bandwidth is from 3.49 GHz to 12.13 GHz, and the fractional bandwidth exceeds 110%. Some parasitic patches are appended to reduce the deviation of resonant frequency under wide-angle incidence. The proposed FSS exhibits an improved stability when the incident angles are in the range from 0° to 60°. The relative simulated and measured results are provided to validate its effectiveness.

1. INTRODUCTION

Frequency selective surface (FSS), which can be regarded as a periodic structure consisting of arranged metallic patches on dielectric layer (s) [1], has been widely used in stealth radome [2], filter [3], and polarizer [4] due to the capability of controlling the transmission and reflection characteristics of incident waves [5]. With the progress of multifunctional aeronautical electronic system which usually contains several antennas with different operating frequencies [6, 7], the need for the ultra-wideband (UWB) FSSs employed in stealth designs of the aircraft is on the rise [8]. In many cases, the angular range of the airborne radome reached 50° or even 60° (e.g., the nose radome) [9], therefore, it is essential that UWB FSSs provide steady frequency response in wide incident angles.

Researchers have made great progress on the wide-angle UWB FSS since Munk indicated that reducing the inter-element spacing of unit cell can improve the angular stability of FSS [1]. Compared with single-layer structure, a multi-layer FSS which has a smaller inter-element spacing was proposed in [10] to provide an UWB bandwidth with the incident angle in the range from 0° to 30°. The structure in [11] utilized the curved slot element to reduce the inter-element spacing, hence its wideband response was capable of remaining stable as the incident angle increases from 0° to 40°. In Ref. [12] and Ref. [13], the UWB FSSs exploiting compact elements possessed a good transmission property when the incident angle was from 0° to 45°. The studies mentioned above utilized various methods; however, the operating performances of these UWB FSSs were still unsatisfactory when the incident angle is over 45°.

In this paper, a UWB FSS with reduced sensitivity to the incident angle is presented. Its -3 dB bandwidth attains 8.64 GHz (3.49–12.13 GHz), which covers the C and X bands, and the fractional bandwidth exceeds 110%. Compared with the UWB FSS in [10], the proposed FSS appends some parasitic patches to enhance the capacitive and inductive effects, then provides the more stable performance at incident angle of 60° for both TE and TM polarizations. The unit cell of the proposed FSS is $0.09\lambda_0 \times 0.09\lambda_0$, where λ_0 corresponds to free space wavelength at the lower cut-off frequency, and the overall thickness is 4 mm. Section 2 of the paper brings out the details of the proposed FSS and the simulation results. In Section 3, the measurement setup for fabricated prototype and related discussions are shown.

2. DESIGN AND SIMULATIONS

Topologies of the proposed FSS in different views are presented in Figure 1, where the unit cells are comprised of three metal layers and two dielectric substrates. The unit cell of top and bottom layers contains a square patch surrounded by four quarter cross parasitic patches (layer 1), while the unit cell of middle layer is a cross metallic line added with four half square parasitic patches (layer 2). Due to the requirement of low transmission loss, the dielectric substrates between the metallic layers is composed of the Rogers RT5880 whose relative permittivity is 2.2 and tangent loss is 0.001. Furthermore, the bandwidth and the insertion loss of the FSS increase as the thickness of the substrate increases. Considering the balance of bandwidth and insertion loss, the optimal thickness is 2 millimeters. When illuminated by the incident waves vertically, the consecutive metallic lines can be represented by the lumped inductor L_1 and L_{e1} while the mutual coupling between separate patches can be represented by the lumped capacitor C_1, C_{e1}, C_{p1}, C_{e2} and C_{p2} as shown in Figure 1(d). The two dielectric substrate
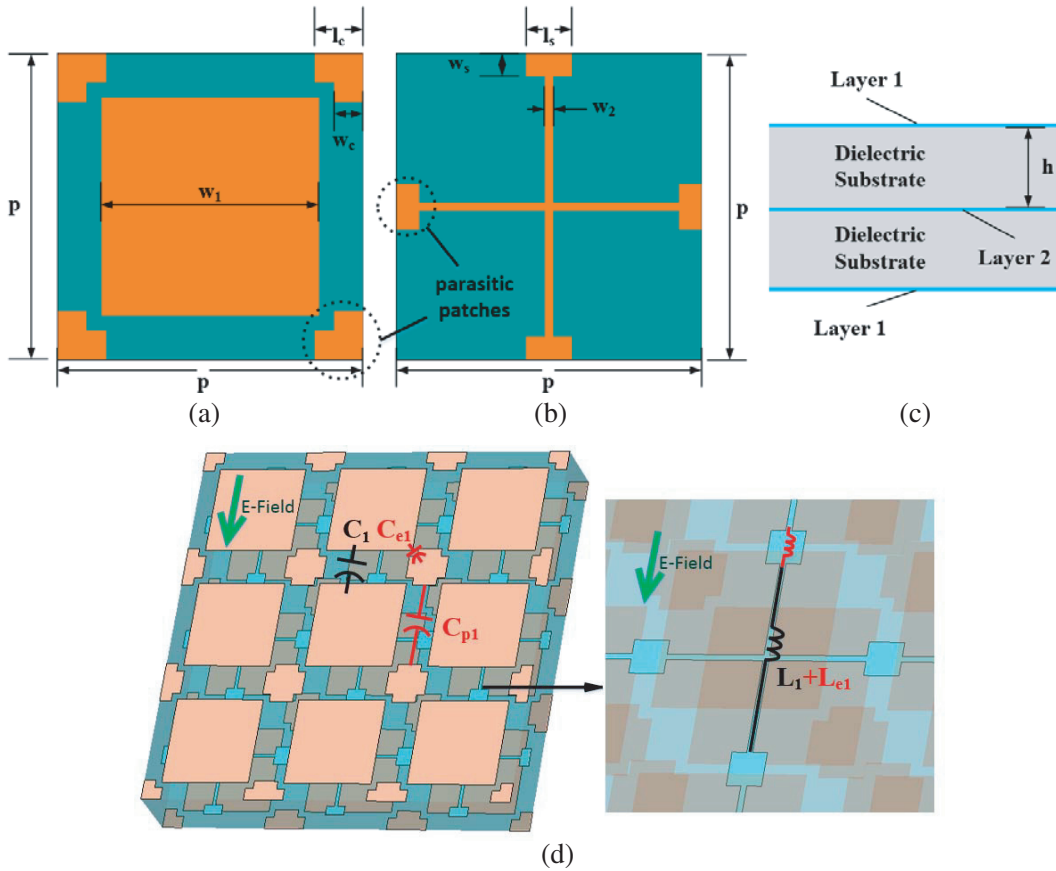

Figure 1. Topology of the proposed FSS in different views. (a) The unit cell of layer 1 in front view. (b) The unit cell of layer 2 in front view. (c) The unit cell in side view. (d) Several unit cells in 3D view.

Table 1. Dimensions of the unit cell of the FSS.

p	w_1	w_c	l_c	w_2	l_s	w_s
8 mm	5.68 mm	0.77 mm	1.28 mm	0.2 mm	1.2 mm	0.6 mm
h	Z_1	C_1	C_{e1}	C_{p1}	L_1	L_{e1}
2 mm	254 Ohm	45.17 fF	22.98 fF	2.35 fF	3.71 nH	0.09 nH

layers can be modeled as the same short piece of transmission line Z_1 whose length equals the thickness of the substrate. All the parameters are given in Table 1. On the basic of the research in [14], the approximate formulae of Z_1, C_1 and L_1 are presented as

$$Z_1 = \frac{Z_0}{\sqrt{(1 - j \tan \delta)\varepsilon_r}} \tag{1}$$

$$C_1 = -\frac{(1 + \varepsilon_r)\,\varepsilon_0 p}{\pi} \ln\left(\sin\frac{\pi p}{s_1}\right) \tag{2}$$

$$L_1 = -\frac{\mu_0 p}{2\pi^2} \ln\left(\sin\frac{\pi w_2}{2p}\right) \tag{3}$$

$$s_1 = \frac{p^2 - w_1^2 - 8 w_c l_c + 4 w_c^2}{4p} \tag{4}$$

where $Z_0 = 377\,\Omega$ is the free space characteristics impedance, ε_r the relative dielectric constant of the substrate, and parameter s_1 represents the average distance between two square patches. Moreover, the capacitance C_{p1} and C_{e1} mainly depend on the width of the cross parasitic patch $2w_c$, the length of the cross parasitic patch $2l_c$ and the average distance between the square patch and the parasitic patch s_{e1}. Meanwhile, the inductance L_{e1} is mainly influenced by the space between the effective width of the square parasitic patch w_{e1}. These parameter can be expressed as

$$C_{p1} = -0.013\frac{(1 + \varepsilon_r)\,\varepsilon_0 p}{\pi} \ln\left(\sin\frac{\pi p}{s_{p1}}\right) \tag{5}$$

$$C_{e1} = -0.324\frac{(1 + \varepsilon_r)\,\varepsilon_0 p}{\pi} \ln\left(\sin\frac{\pi p}{s_{e1}}\right) \tag{6}$$

$$L_{e1} = -0.012\frac{\mu_0 p}{\pi^2} \ln\left(\sin\frac{\pi l_s w_s}{p^2}\right) \tag{7}$$

$$s_{p1} = \frac{2 w_c\,(p - 2l_c) + (p - w_1 - 2w_c)\,(p - 2w_c)}{p - w_1} \tag{8}$$

$$s_{e1} = \frac{\displaystyle\int_0^{\sqrt{2}l_c/2}\left[-x + \frac{\sqrt{2}\,(p - w_1)}{2}\right]dx + \int_{\sqrt{2}l_c/2}^{\sqrt{2}l_c}\left(x - \frac{p - w_1 - 2w_c}{2}\right)dx}{\sqrt{2}l_c}. \tag{9}$$

Further, Figure 2 presents the equivalent circuit model (ECM) of the proposed FSS and gives a comparison of the S-parameters evaluated by full-wave and ECM simulations. It can be observed that
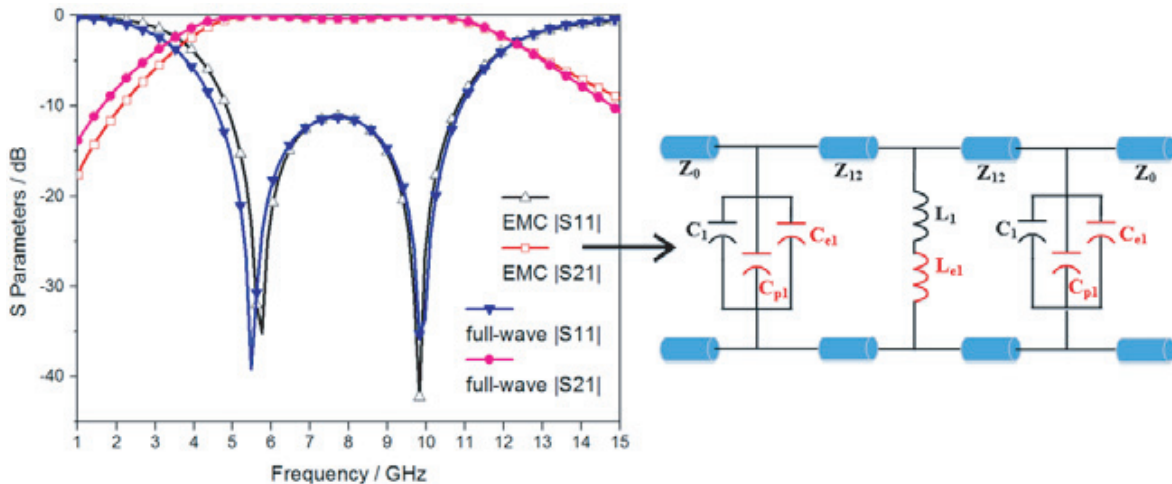

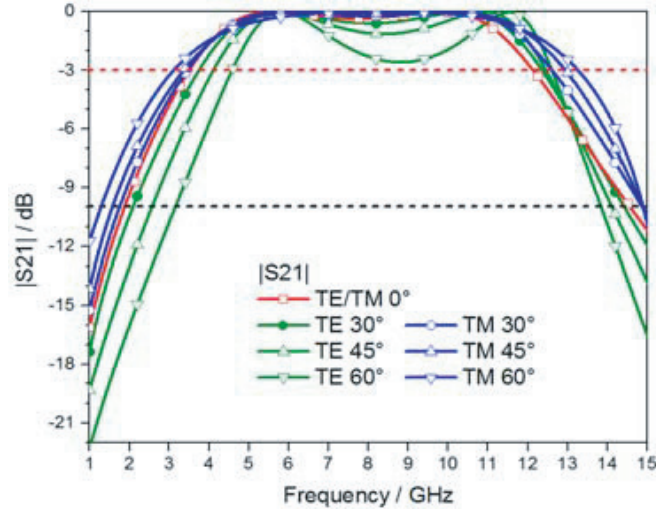**Figure 2.** The reflection and transmission coefficients by full-wave/ECM simulations.

Figure 3. Transmission coefficients with various incident angles for TE/ TM polarizations.

the proposed FSS exhibits two resonant frequency points (5.62 GHz and 9.84 GHz), and the results from full-wave and ECM simulations show a good consistency. The parasitic patches provide additional capacitance and inductance, which are red-highlighted in the ECM, to reduce the resonant frequency deviations at wide-angle incidence. That will be discussed in the following paragraphs.

The transmission coefficients of the proposed FSS with various incident angles for TE/TM polarizations are shown in Figure 3. The proposed FSS features lower sensitivity to the incident wave with various incident angles for both TE and TM polarizations, and keep a steady performance in the whole operating bandwidth. The -3 dB bandwidth of the presented FSS is 8.64 GHz (3.49 GHz–12.13 GHz), covering the C and X bands. The minimum pass band insertion loss is merely 0.01 dB at 9.84 GHz, and the insertion loss from 4.29 GHz to 11.23 GHz is less than 1 dB. More than 10 dB attenuation is obtained when the frequency is lower than 1.88 GHz or higher than 14.54 GHz. Under the circumstance where the electromagnetic waves incident at an angle θ, the impedance of the FSS is required to multiply a coefficient $\cos \theta$ by the TM mode incident wave, and this coefficient becomes $1/\cos \theta$ when the wave is TE mode. Therefore, when the incident wave is TM mode, the bandwidth will increase along with the incident angle, on the contrary to the TE wave. In the worst case (at 60° for the TE polarization), the operating bandwidth still attains 8.06 GHz, and the fractional bandwidth exceeds 94%. Under the TM polarization, the widest bandwidth attains 10.25 GHz, and the fractional bandwidth exceeds 125%.

As mentioned above, the proposed FSS are added with some parasitic patches, which are labelled in Figure 1(a) and Figure 1(b), to strengthen the coupling excitation. Compared to TM-polarized incident waves, TE-polarized incident waves are more affected by wide angles. So the Figure 4 shows the surface currents of the proposed FSS at two resonant frequencies for TE polarization. The parasitic patches are appended to provide additional capacitive and inductive effects, and all of them excite the strong surface currents when illuminated by the wide-angle incidence. Several simulated experiments proved that the enlargement of the parasitic patches will result in the increase of the additional coupling strength. But when these parasitic patches are too large, they will change the capacitance/inductance of the original patches, then reduce the working bandwidth and increase insertion loss. It is significant that taking a optimized parasitic patches size to ensure the frequency response at wide angle is stabilized, while the frequency response at vertical incidence almost maintain unchanged.

The main difference between the proposed FSS and the FSS in [10] is the parasitic patches. In order to illustrate the function of parasitic patches that can reduce the resonant frequency deviation at wide incident angle, the simulated reflection coefficients of the proposed FSS and the FSS in [10] are presented in Figure 5(a). As shown in Figure 5(a), each FSS has two resonant frequencies (the first one and the second one), which more or less shift to the higher frequency at the incident angle of 60°. It is obviously that the frequency deviation of the proposed FSS is less than that of the FSS in [10]. The
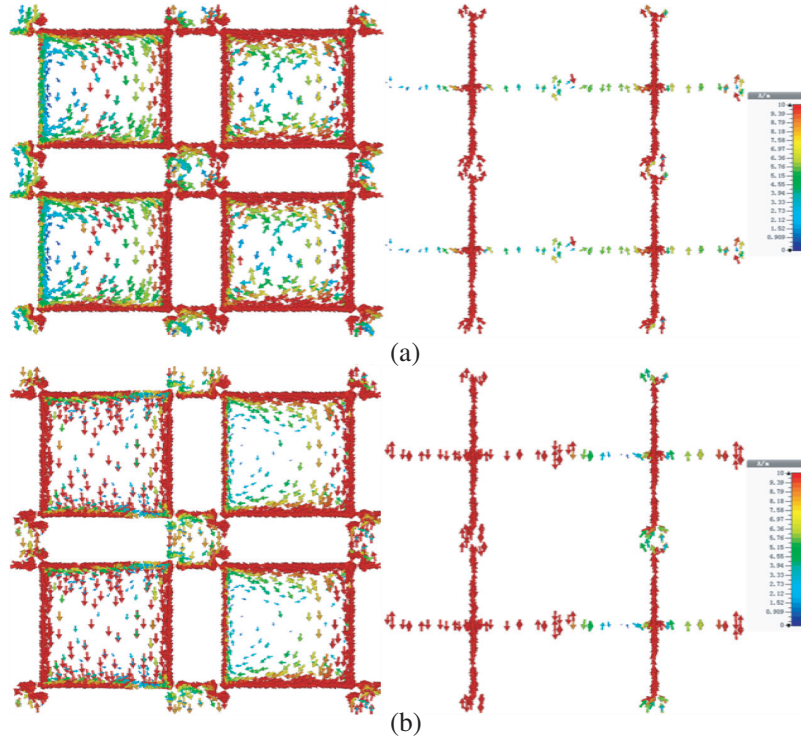
Figure 4. Surface currents under 60° incidence for TE polarization. (a) At 5.92 GHz. (b) At 11.74 GHz.
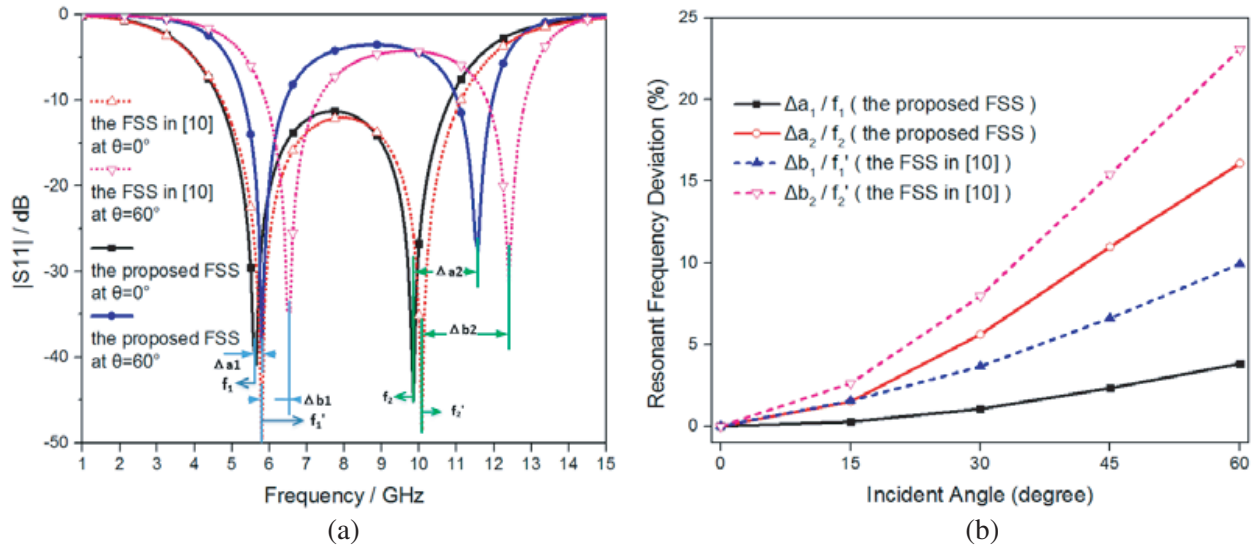

Figure 5. Comparison between the proposed FSS and the FSS in [10]. (a) Reflection coefficients of at 0° and 60°. (b) Resonant frequency deviations at various incident angles.

further simulated results of the resonant frequency deviations in various incident angles are provided in Figure 5(b), where Δa_1 and Δb_1 represents the first resonant frequency deviation of the proposed FSS and the FSS in [10] while Δa_2 and Δb_2 corresponds to the second resonant frequency. These deviation values are divided by the resonant frequencies at the vertical incidence, then the relative percentages of frequency deviations is obtained. The curves show that the deviations of both the first and second resonant frequencies are depressed due to the parasitic patches, especially for the wide-angle incidence.

3. EXPERIMENT AND RESULTS

The proposed FSS is fabricated with a total dimension of $320\,\mathrm{mm} \times 320\,\mathrm{mm} \times 4\,\mathrm{mm}$ (40×40 unit cells). Figure 6 shows the FSS sample and the experimental environment, where a vector network analyzer (Agilent N5230C over frequencies from $300\,\mathrm{kHz}$ to $20\,\mathrm{GHz}$) and two diagonal horn antennas are used. The FSS sample is fixed on a bracket in a microwave anechoic chamber. The transmitting and receiving antennas are placed on both sides of the sample to measure the transmission coefficient.
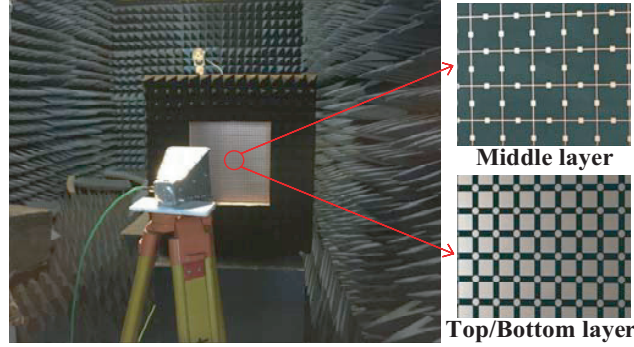

Figure 6. Photograph of the FSS sample and the experimental environment.

Figure 7 shows the measured frequency responses for TE and TM polarizations at three different incident angles, with the simulated curves given again for comparison. The measured pass band is deviated to a little higher frequency, so the range of the figure starts at $3\,\mathrm{GHz}$ for the clarity. The measured bandwidth becomes narrower compared with the simulated one due to the inherent tolerances of the FSS sample in the fabrication process. When the incident wave is TM mode, the bandwidth will be proportional to the angle of incidence. Under the TE polarization, the resonant frequencies deviation make the bandwidth narrower, and the sinking of the pass-band curve is similar to the simulated one. The experimental results agree well with the simulated ones.
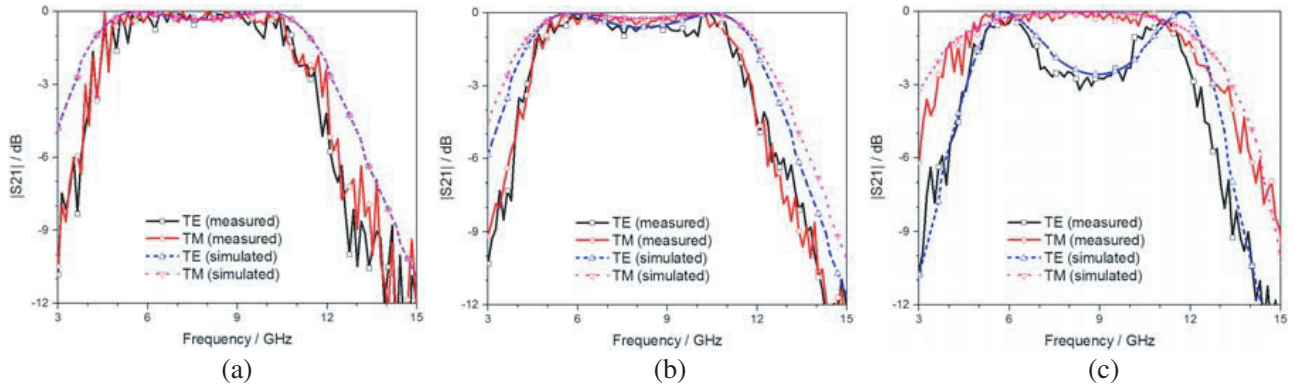

Figure 7. Measured and simulated frequency responses of the FSS with (a) $\theta = 0°$, (b) $\theta = 30°$, (c) $\theta = 60°$.

4. CONCLUSIONS

In this paper, an ultra-wide FSS for the wide-angle incidence is proposed. By studying the surface currents and the reflection coefficients, it can be found that the parasitic patches depress the resonant frequency deviations caused by wide-angle incidence effectively. The experimental results show a good consistency with the simulated data. Therefore, the proposed FSS shows the potential value in the stealth design of ultra-wideband radio frequency integrated system on aircraft.

ACKNOWLEDGMENT

REFERENCES

1. Munk, B. A., *Frequency Selective Surfaces: Theory and Design*, Wiley, New York, 2000.

2. Baskey, H. B. and M. J. Akhtar, "Design of flexible hybrid nanocomposite structure based on frequency selective surface for wideband radar cross section reduction," *IEEE Trans. Microw. Theory*, Vol. 65, No. 6, 2019–2029, 2017.

3. Zhang, J. C., Y. Z. Yin, and J. P. Ma, "Design of narrow band-pass frequency selective surfaces for millimeter wave applications," *Progress In Electromagnetics Research*, Vol. 96, No. 4, 287–298, 2009.

4. Sharifian, M. and M. Mollaei, "Narrow-band configurable polarization rotator using frequency selective surface based on circular substrate integrated waveguide cavity," *IEEE Antennas & Wireless Propagation Letters*, Vol. 16, 1923–1926, 2017.

5. Lorenzo, J., A. Lazaro, D. Girbau, R. Villarino, and E. Gil, "Analysis of on-body transponders based on frequency selective surfaces," *Progress In Electromagnetics Research*, Vol. 157, 133–143, 2016.

6. Tiemann, J., F. Schweikowski, and C. Wietfeld, "Design of an UWB indoor-positioning system for UAV navigation in GNSS-denied environments," *IEEE International Conference on Indoor Positioning and Indoor Navigation*, 2015.

7. Izabela, G., L. Vinay, G. Leonid, A. Donald, and B. Frank, "Analyses and simulations for aeronautical mobile airport communications system," *Integrated Communications Navigation and Surveillance*, 2016.

8. Syed, I. S., Y. Ranga, and L. Matekovits, "A single-layer frequency selective surface for ultrawideband electromagnetic shielding," *IEEE Trans. Electromagn. Compat.*, Vol. 56, No. 6, 1404–1411, 2014.

9. Wang, J., G. Guo, and H. Zheng, "Characteristic analysis of nose radome by aperture-integration and surface-integration method," *IEEE International Workshop on Microwave and Millimeter Wave Circuits and System Technology*, 2012.

10. Zhou, H., S. B. Qu, and J. F. Wang, "Ultra-wideband frequency selective surface," *Electron. Lett.*, Vol. 48, No. 1, 11–13, 2012.

11. Kesavan, A., R. Karimian, and T. A. Denidni, "A novel wideband frequency selective surface for millimeter-wave applications," *IEEE Antennas & Wireless Propagation Letters*, Vol. 15, 1711–1714, 2016.

12. Ramprabhu, S., M. Balaji, and K. Malathi, "Polarization-independent single-layer ultra-wideband frequency-selective surface," *Journal of Electromagnetic Waves and Applications*, Vol. 9, No. 1, 93–97, 2015.

13. Li, D., T. W. Li, and R. Hao, "A low-profile broadband bandpass frequency selective surface with two rapid band edges for 5G near-field applications," *IEEE Trans. Electromagn. Compat.*, Vol. 59, No. 2, 670–676, 2017.

14. Al-Joumayly, M. A. and N. Behdad, "A generalized method for synthesizing low-profile, band-pass frequency selective surfaces with non-resonant constituting elements," *IEEE Trans. Antennas Propag.*, Vol. 58, No. 12, 4033–4041, 2010.